ENGINEERING

Damage-tolerant 3D-printed ceramics via conformal coating

Seyed Mohammad Sajadi[1], Lívia Vásárhelyi[2], Reza Mousavi[3], Amir Hossein Rahmati[4], Zoltán Kónya[2,5]*, Ákos Kukovecz[2], Taib Arif[6], Tobin Filleter[6], Robert Vajtai[1,2], Peter Boul[7], Zhenqian Pang[8], Teng Li[8]*, Chandra Sekhar Tiwary[9]*, Muhammad M. Rahman[1]*, Pulickel M. Ajayan[1]*

Ceramic materials, despite their high strength and modulus, are limited in many structural applications due to inherent brittleness and low toughness. Nevertheless, ceramic-based structures, in nature, overcome this limitation using bottom-up complex hierarchical assembly of hard ceramic and soft polymer, where ceramics are packaged with tiny fraction of polymers in an internalized fashion. Here, we propose a far simpler approach of entirely externalizing the soft phase via conformal polymer coating over architected ceramic structures, leading to damage tolerance. Architected structures are printed using silica-filled preceramic polymer, pyrolyzed to stabilize the ceramic scaffolds, and then dip-coated conformally with a thin, flexible epoxy polymer. The polymer-coated architected structures show multifold improvement in compressive strength and toughness while resisting catastrophic failure through a considerable delay of the damage propagation. This surface modification approach allows a simple strategy to build complex ceramic parts that are far more damage-tolerant than their traditional counterparts.

INTRODUCTION

Ceramic materials are widely used in structural applications because of their outstanding environmental resistance, low density, and high strength properties. Also, the remarkable biocompatibility of ceramics has attracted them in many biomedical applications such as bone substitutes, tissue engineering scaffolds, dentals, surgical tools, and instruments. However, they display near-zero plastic deformation and low toughness due to a limited ability to resist fracture. Even the slightest defects or flaws introduced during processing can substantially compromise the strength and toughness of the ceramic. Thus, this inherent brittleness or poor toughening mechanism limits ceramic materials application in many structural components even at ambient conditions.

Nature, on the other hand, overcomes such limitations by developing ceramic-based composites through multiple length-scale complex architectures with internalized designs, where the optimized composition of hard minerals is packaged with soft organic phases in a layer-by-layer assembly. There are many examples of lightweight ceramic-based composite structures with excellent strength and toughness in nature made of components that have relatively low mechanical properties. For example, nacre from mollusk shell is composed of ~95 volume % of fine layered brick-like aragonite ($CaCO_3$) platelets (<900 nm) bonded by biopolymers (5 volume %) in a three-dimensional (3D) brick-and-mortar assembly and has a fracture toughness roughly three orders of magnitude higher than its constituents (1–3). Similarly, bone is a hierarchical architected nanocomposite of a soft matrix (collagen fibrils, ~20 to 30%) and hard mineral nanocrystals (plate-shaped hydroxyapatite, ~60%) arranged in a periodic, staggered array along the fibrils (4–6). Despite very high mineral content of these ceramic-based composites, they can arrest crack propagation and avoid catastrophic failure through a combination of various toughening and strengthening mechanisms at many size scales (7–9). Typically, the microstructure of these natural composites is designed in a different architected orientation, while the hard ceramic surface layer provides high fracture strength and a soft proteinaceous subsurface allows large deformation.

By mimicking the length scales and hierarchy of these biological materials, several research efforts have focused on developing architected damage-tolerant lightweight engineered ceramic structures at the nano- and microscale (10–16). Typically, synthetic ceramics have been developed using biomimetic mineralization, layer-by-layer deposition, solution casting, self-assembly, freeze casting or ice templating, and additive manufacturing to enhance the toughness of engineered materials (17–20). However, most of these processes are time consuming and are only capable of developing nano- and microscale ceramic-based composite structures. While ice templating (21) and additive manufacturing (22–26) are promising methods to develop scale-independent structures, there are many challenges that must first be addressed, such as materials limitations, controlled assembly, and surface quality. Hence, development of damage-tolerant ceramic-based architected structures at the macroscale still remains challenging.

The bioinspired concept has been implemented for designing other engineered materials such as laminated glass and double-network hydrogel (27–30). In these structures, the primary disadvantage of the stiff and/or brittle phase (low resistance to fracture under loads) has been overcome by forming interlinked polymer-ceramic structures. As a result, combinatorial benefit of high strength and toughness has been achieved, allowing these structures to be

[1]Department of Materials Science and NanoEngineering, Rice University, Houston, TX 77005, USA. [2]Interdisciplinary Excellence Centre, Department of Applied and Environmental Chemistry, University of Szeged, Szeged, Hungary. [3]ANSYS Inc., Houston, TX 77094, USA. [4]Department of Mechanical Engineering, University of Houston, Houston, TX 77204, USA. [5]MTA-SZTE Reaction Kinetics and Surface Chemistry Research Group, University of Szeged, Szeged, Hungary. [6]Department of Mechanical and Industrial Engineering, University of Toronto, Toronto, Ontario, Canada. [7]Aramco Americas, Houston, TX 77002, USA. [8]Department of Mechanical Engineering, University of Maryland, College Park, MD 20742, USA. [9]Metallurgical and Materials Engineering, Indian Institute of Technology Kharagpur, West Bengal, India.
*Corresponding author. Email: konya@chem.u-szeged.hu (Z.K.); lit@umd.edu (T.L.); chandra.tiwary@metal.iitkgp.ac.in (C.S.T.); mr64@rice.edu (M.M.R.); ajayan@rice.edu (P.M.A.)

used in several applications such as auto windshields, hurricane-proof building windows, blast-resistant windows, and synthetic connective tissues (*27*, *28*, *30*). Nevertheless, this particular concept can be further stretched for the development of innovative material design in terms of structural arrangement and/or configuration. Specifically, damage tolerance in ceramic-based structures by simply and cost-effectively wrapping a thin polymer film around, while ensuring no infiltration or composite formation, has not been realized yet. Although molten glass glaze in traditional ceramics has been used with the intention of filling surface cracks and achieving a smooth surface, such coating layers do not improve, if not deteriorate, the inherent brittleness of the structure.

Here, we report a far simpler fabrication of damage-tolerant architected ceramic structures via stereolithography (SLA) 3D printing followed by a conformal polymer micro-coating that externalizes the soft phases entirely from the ceramic structures. A well-known architected geometry called schwarzite (*31*) has been developed using commercial silica-filled preceramic polymer, the polymer was completely pyrolyzed to create a fully ceramic structure, and then the ceramic structure was conformally coated with a thin layer of flexible epoxy polymer. The mechanical behavior of the coated architected ceramic has been analyzed by a uniaxial compression test and compared to the behavior of uncoated ones. The crack initiation, propagation, and arresting of these architected structures have been investigated by in situ micro–computed tomography (micro-CT) under different compression loads. Then, finite element method (FEM) based on the continuum plasticity-based damage model was performed to understand the damage propagation of the architected structure in compression load due to the conformal coating. Furthermore, we carried out atomistic modeling to reveal the strengthening and toughening mechanism of the epoxy-coated ceramic under uniaxial compression loading. Last, we analyzed different architectures and geometries to reveal the effect of coating for the general applicability regardless of the core ceramic structures.

RESULTS

Schwarzites are 3D carbon-based periodic networks with zero mean curvature and negative Gaussian curvatures (*31*, *32*). They have excellent mechanical properties and diverse electronic properties with tunable cell size and shape (*31*, *32*). Thereby, this molecular structure has received attention to develop energy-absorbing materials in macroscopic scale that can withstand large deformation without fracture. Hence, we investigated the effect of the polymer coating on the macroscale mechanical behavior of ceramic structures with schwarzite architecture (primitive). Macroscale schwarzite structures were fabricated using SLA 3D printing of silica-filled (SiO_2) preceramic polymer followed by pyrolysis (up to 1271°C) to burn out the binding polymer completely and create a fully ceramic structure with uniform volumetric shrinkage (~15%) (Fig. 1, A and B; fig. S1; and table S1). The ceramic schwarzite structure was then coated using the epoxy polymer by a dipping method and cured with ultraviolet (UV) light. Note that the tensile modulus of the 3D-printed sintered ceramic is around 50 times higher than that of epoxy (material properties are provided in tables S2 and S3). Figure 1B shows two different 3D-printed ceramic schwarzite samples: Sample I (without coating) is used as a reference for comparison, and sample II is dip-coated in epoxy and cured under UV light, while Fig. 1C shows the schematic of their distinct mechanical

behavior in quasi-static compression loading. Scanning electron microscopy (SEM) was used to analyze the topographical features and thickness of the polymer coating. Figure 1 (D and E) shows that the whole ceramic surface was uniformly coated with a ~70- to 100-μm-thick epoxy layer. Furthermore, the epoxy layer is shown to effectively enter the ceramic surfaces and fill the pores on the surfaces (Fig. 1, D to G, and fig. S2). The coating did not infiltrate the struts and form a composite material that has been confirmed by silica-rich zone along the cross section, as obtained from elemental mapping study of a coated strut cross section (fig. S3). As was observed, the soft polymer coating forms a coherent interface with the hard ceramic through effective physical interlocking.

It is well known that structural toughening mechanisms are classified into intrinsic and extrinsic categories (*33–35*). Intrinsic toughening mechanisms work mostly ahead of the crack tip and are effective against crack initiation and propagation by enlarging the plastic zone, similar to the toughening mechanism in ductile materials (e.g., metal alloys). On the other hand, the primary source of extrinsic toughening mechanisms in brittle materials is located behind the crack tip. They do not affect the crack initiation; instead, mechanisms such as crack arrest, bridging, deflection, and twisting reduce the strain energy release rate at the crack tip in nano- and microscales and prevent crack growth or propagation. To determine the effect of a micro-coating on the mechanical properties of brittle ceramic, we conducted a uniaxial compression test on both coated and uncoated ceramic schwarzites (Fig. 2). Because ceramics are inherently brittle due to the lack of mobile dislocations, the uncoated sample expectedly failed at a low strain level. However, the polymer micro-coating significantly increased the load-bearing capacity of the sample, as shown from the typical stress-strain behavior in Fig. 2A. The fracture of the coated ceramic features the progressive fragmentation of the unit cells in the model, while the coating acts as a support layer to hold the broken ceramics together. The corresponding stress-strain curve of the coated structure features a quasi-linear elastic region at small deformation, followed by a plateau of the curve and then a sudden drop of stress, indicating the failure of the structure. It is shown that the fracture initiates from the breaking of the solid edges of a unit cell and further advances to fracture the connector between the unit cells (movie S1). Hence, localized or compartmentalized crack propagation of unit cells helps the structures to withstand even after failures of several unit cells. Thus, the progressive fractures due to the compartmentalization results in controlled failure of the whole structure. Also, the damage progression is delocalized by the crack arrest and deflection in the polymer-ceramic interfaces, resulting in higher energy dissipation within the materials and enhancing their overall toughness. Figure 2B represents the specific energy absorption in log scale and fracture strain in linear scale for both the samples. Uncoated architected ceramic fails catastrophically at low strain (~2%) with an average specific energy absorption of ~23 J/g cm³, while a thin layer of coating enhances their fracture strain and specific energy absorption by about 13 times (~30%) and 77 times (~1780 J/g cm³) higher compared to the uncoated ceramic, respectively. Several snapshots were taken at different strain levels during the test to understand the failure of the samples. Once the crack is generated in the uncoated sample, it easily propagates through the whole structure and leads to catastrophic failure and disintegration of the ceramic structure into pieces (Fig. 2C and movie S1). On the other hand, the thin layer of coating resists catastrophic failure and
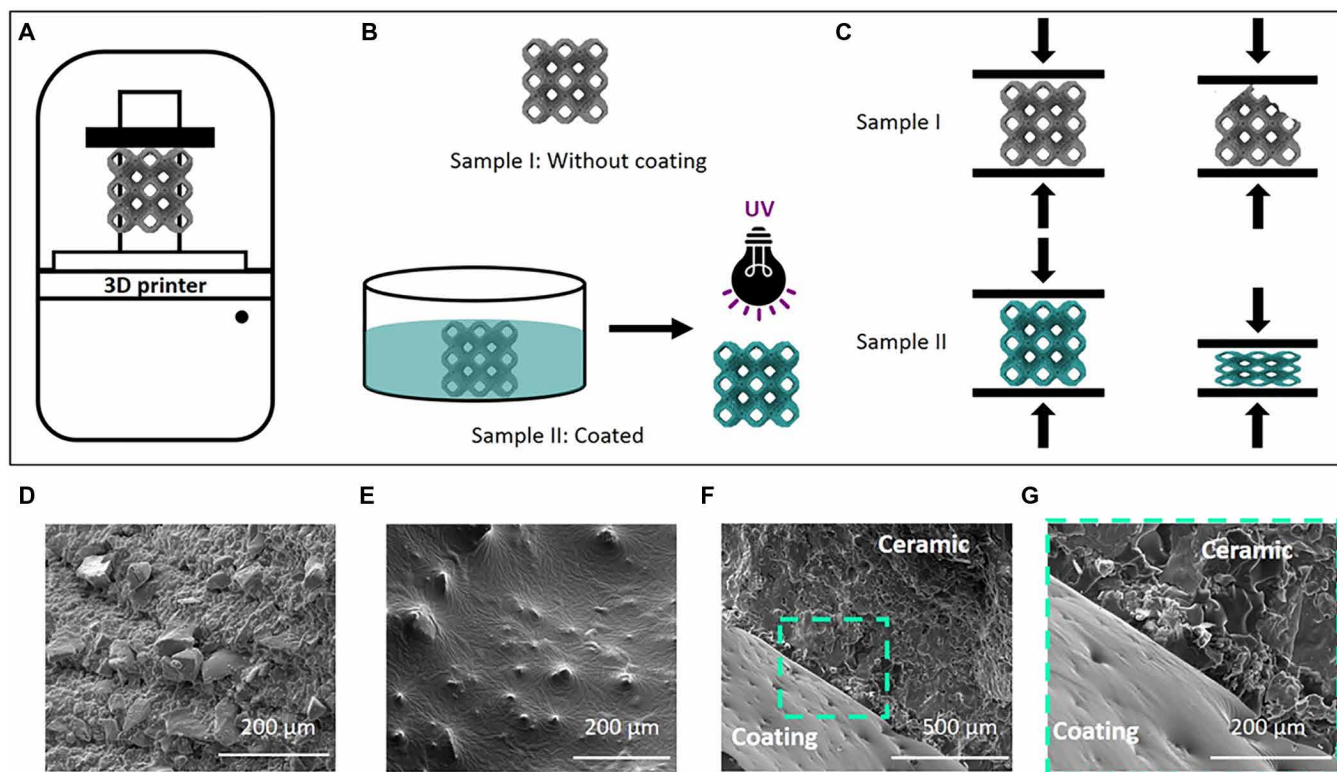
Fig. 1. Fabrication and morphology of polymer-coated architected ceramic. (**A**) Printing ceramic schwarzite samples with an SLA 3D printer. (**B**) Sample I (uncoated ceramic) is fabricated using ceramic without any further processing. Sample II (coated ceramic) is dipped in epoxy and placed under UV light to cure the epoxy and form a thin layer of conformal coating on the whole surface. (**C**) Schematic of quasi-static compression studies on both samples. Sample I broke catastrophically, while sample II showed layer-by-layer deformation with a progressive failure. (**D**) SEM image of the surface topography of uncoated ceramic. (**E**) SEM image of the surface topography of coated ceramic that shows the uniformity of the coating. (**F** and **G**) SEM images of cross section show the polymer-ceramic interface and thickness of the coating (~70 to 100 μm) at a low and high magnification. Figure S2 provides more information about the morphology and thickness. Photo credit: Seyed Mohammad Sajadi, Rice University.

disintegration, and we observed a compartmentalized deformation in the coated samples (Fig. 2D and movie S1). Furthermore, as the polymer coating fills the surface micropores of the ceramic structure and forms a coherent interface with the ceramic through uniform physical interlocking, the cracks initiated from the ceramic phases can be effectively arrested and deflected during the fracture process (Fig. 2, E to G). Earlier, designing weakly interacting interfaces within material systems at both the atomic scale (*36*) and microscale (*37*) has been shown to improve the toughness of composites by deflecting the cracks along the weakly interacting interfaces. Clegg *et al.* (*37*) reported that embedding weakly interacting interfaces within ceramic composites can increase fracture toughness fourfold and substantially increase the work for failure. The flexible polymer coating can be deformed substantially in the wake of the crack opening, which can effectively reduce the driving force of the crack by decreasing the strain energy release rate at the tip. Similar behavior has been observed in the inner and outer struts of the whole structure. In addition, while approaching the failure strain, the fragmented ceramic was confined and held together by the polymer coating and thus provides compressive strength and deformations.

To further demonstrate the versatile applicability of the polymer coating in improving the mechanical performance of ceramic structures, we 3D-printed solid ceramic structures with a cylindrical shape and coated them using the similar method. We next carried out uniaxial compression test of two types of samples: solid cylindrical ceramic structures with and without polymer coating. We found that the toughness and fracture strain of the coated structure are ~2.5 times and ~4.5 times higher than those of the uncoated one (fig. S4). It is evident that the architected structures with a coherent polymer coating show significantly more enhancement in toughness and fracture strain than their solid counterparts, which can be attributed to the increased surface area of the architected structures. Thus, we confirm a substantial architectural advantage on the effect of coating. To confirm the architectural benefits, we also conducted compression tests on other architected structures including primitive and gyroid schwarzites (primitive: P688 and gyroid: G8bal). Similar behavior with pronounced differences was observed in each case for coated and uncoated architected structures (fig. S5). These behaviors confirm that the efficacy of this method depends on the porosity and architecture of the sample.

Next, for a better understanding of crack propagation in both samples and toughening mechanisms in the coated samples, we carried out in situ micro-CT imaging at different compressive loads. Figure 3 shows the CT images of both samples, where the gray color represents the initial condition of the structures and the color shift from yellow to red indicates the increase of the compressive load (note that the same color indicates higher load for coated samples).
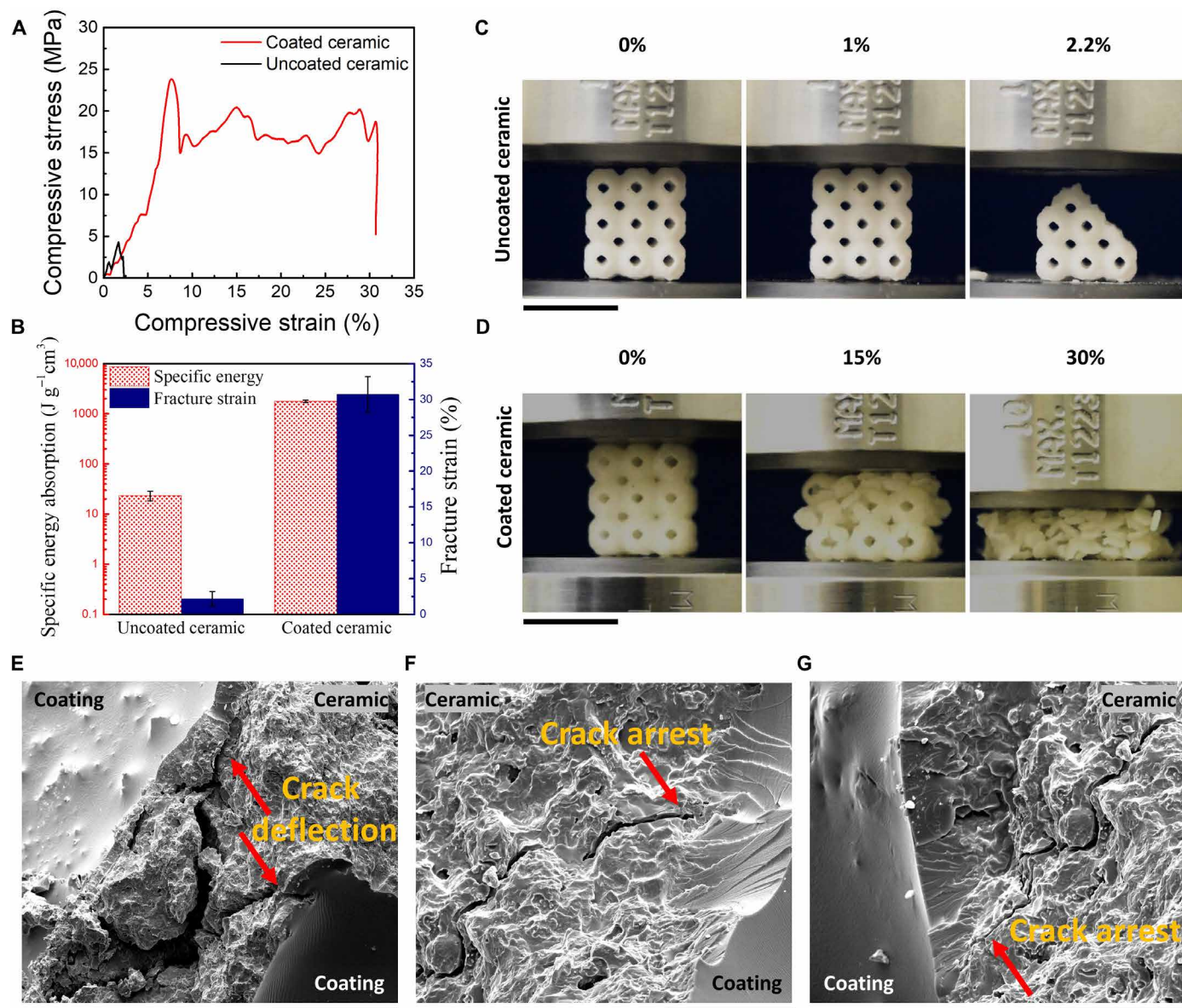
Fig. 2. Role of polymer coating on compressive strength and deformation behavior of architected ceramic. (A and B) Typical compressive stress-strain behavior of uncoated and coated ceramic schwarzites. The dip-coating of the ceramic in epoxy effectively enhances the strength and toughness of the architected structure. The epoxy coating leads to a significant increase in the compressive toughness of the structure. (C) A series of snapshots from compressive tests shows the catastrophic failure of uncoated ceramic at low strain values. Scale bar, 1 cm. (D) The progressive failure through a layer-by-layer deformation for the coated ceramic explains the role of coating, which is unusual in brittle material like ceramic. Scale bar, 1 cm. (E) SEM shows the crack deflection in the coated ceramic after compression testing. Scale bar, 500 μm. (F and G) Crack was initiated and propagated through the inner and outer struts in the architected structures, and crack arrest was observed in the ceramic-polymer interfaces as shown by the red arrow. Scale bar, 200 μm. Photo credit: Seyed Mohammad Sajadi, Rice University.

While applying compression load on the uncoated samples, we observed several small cracks that connected and started to propagate through the whole structure with the increasing load, leading to catastrophic failure at a low strain level (Fig. 3A). The crack propagation can easily be seen in the magnified CT images of Fig. 3A (bottom line). However, we observed a considerable difference in the coated samples during in situ compressive loading and figured out that the conformal micro-coating plays a crucial role in avoiding crack interconnection. The crack was initiated by applying a compressive load similar to the uncoated sample; however, the soft

polymer coating can effectively arrest at the ceramic-polymer interfaces and deflect the crack initiated inside the ceramic. This is in good agreement with the SEM results of Fig. 2 (E and F). As a result, the whole structure retained continuity. (Details of micro-CT scan imaging are described in Materials and Methods and movie S2.)

To offer qualitative insight of the influence of polymer coating on the damage evolution in the ceramic structure, we carried out a computational study using a plastic damage model (Fig. 4). Using a finite element model (FEM), which accounts for both concepts of plasticity and damage, we calibrated damaged and plastic material
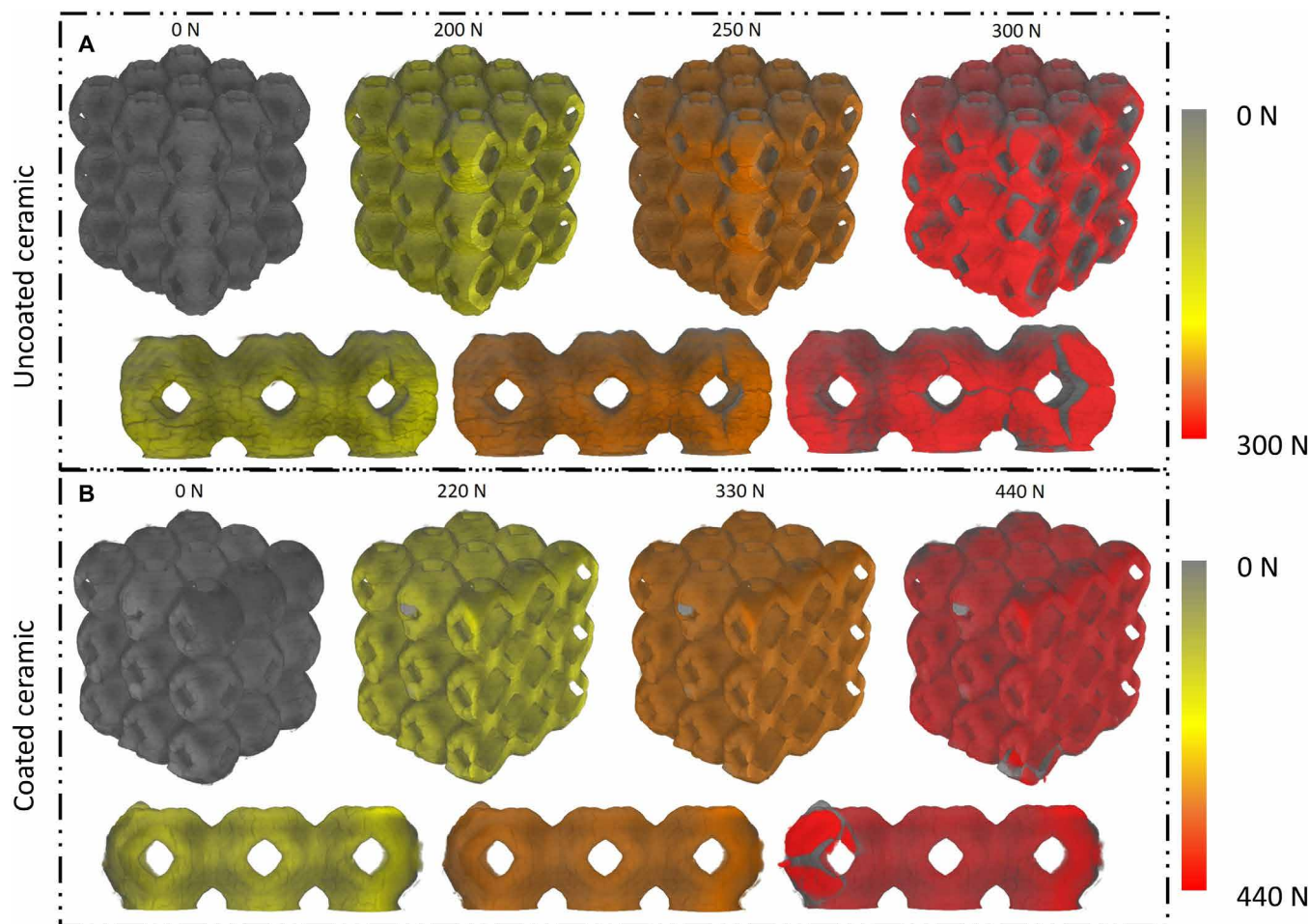
Fig. 3. Toughening mechanism illustrated by in situ micro-CT images. (A) CT scan images of uncoated ceramic under various load levels and load increase from gray to red color. A higher-magnification image shows how the crack propagates and is connected to each other under progressively higher load levels. (**B**) CT scan images of coated ceramic under various load levels. The effectiveness of coating in crack propagation of the ceramic samples under different loads is demonstrated.

properties in a way that failure of the ceramic without coating occurs in about 2% strain. We next compared the damage evolution in the same model and a model with a polymer coating. Figure S7, tables S4 and S5, and movie S3 explain the FEM modeling details. Figure 4 shows the contours of the damage variable for both samples (uncoated and coated ceramic) under low and high strain. The damage evolution is characterized by a damage variable, ranging from zero (undamaged) to one (fully damaged). In actual simulations, we set the upper limit of the damage variable to be 0.9 to guarantee the convergence of numerical simulation. The FEM analysis was carried out on a single unit cell of both samples (Fig. 4A). Figure 4B shows that the damage contours look very similar for both the coated and uncoated samples at low strain, although the uncoated ceramic exhibits slightly greater damage in some locations. Specifically, the damage variable for the uncoated sample can reach as high as 0.155 at 0.7% strain, relatively higher than that of the coated one (~0.111). This indicates that the coating has a partial effect on delaying crack initiation. However, damage in the uncoated sample is significantly greater than that of coated ceramic at a high strain level (Fig. 4C). Damage contour of the ceramic shows that damage has reached its maximum of 0.9 in a path (crack region), which has been illustrated with red, while a far milder damage is seen in the

ceramic with coating, where damage variable hardly reaches the value of 0.6. The section views show damage, and plastic strain in the sample with the coating is more distributed compared to ceramic without the coating where damage is seen to be more concentrated. Magnified views show the crack region through thickness of the ceramic. A higher value of localized plastic strain results in crack and brittle failure of the ceramic, while under the same loading, much less damage and plastic strain is reported for the sample with coating. The cracked region is completely aligned with the CT images (Fig. 3), indicating that the simulation matches the experimental results. From these results, we conclude that polymer coating does not considerably affect damage initiation but does considerably delay the damage propagation and structural failure.

Last, we carried out molecular dynamics simulations to shed further light on the toughening and strengthening mechanisms in the coated ceramic under uniaxial compression (Fig. 5 and figs. S8 and S9). After getting the stable atomic structure of the epoxy and ceramic, we coated the epoxy on the surface of the ceramic and relax the composite structure for sufficient duration of time in the isothermal-isobaric (NPT) ensemble (details are provided in Materials and Methods), which corresponds to the formation of the coated ceramic in the experimental fabrication. Note that the surface of uncoated
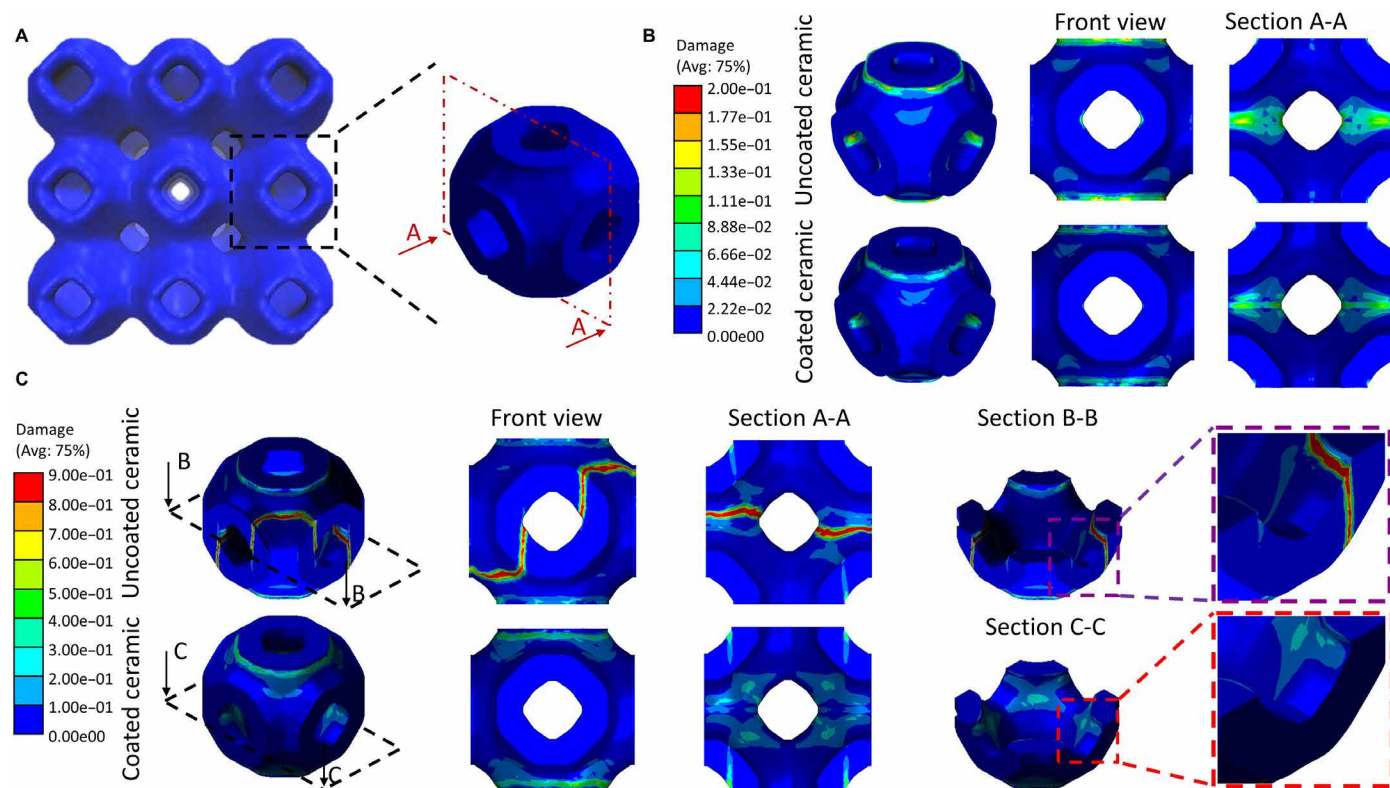
Fig. 4. FEM in the plastic region. (**A**) FEM analysis is performed by taking a unit cell of the structure and calculating principal stress and strain. For better presentation, the unit cell was sectioned from the middle. Damage contours for coated and uncoated samples were shown for (**B**) low strain (about 0.7%) and (**C**) high strain (about 1.75%). Under low strain, damage contours in coated and uncoated samples are similar; however, under high strain, damage in uncoated ceramic is considerably greater than that in the coated sample.

ceramic is naturally rough due to the internal atomic structure of amorphous silica (Fig. 5B, top), while such surface fluctuations of the ceramic are filled by the epoxy during the coating process (Fig. 5A, left). Compressive loading was applied in the x direction to both the coated and uncoated ceramic. The right panel in Fig. 5A shows the stress component (σ_{xx}) of the per-atom stress tensor in the coated ceramic under a uniaxial compressive strain of 15%, while the bottom panel in Fig. 5B shows the same stress component in the uncoated ceramic under a uniaxial compressive strain of 7%. The stress in the ceramic is higher than that in the epoxy, essentially because the ceramic is substantially stiffer than the epoxy and the load is dominated by the ceramic.

Figure 5C shows the compressive stress in the coated and uncoated ceramic as a function of the applied uniaxial compressive strain. It is evident that the coated ceramic has a higher compressive strength (~82 MPa) than the uncoated ceramic (~57 MPa). Furthermore, the energy absorption, corresponding to the area underneath the stress-strain curve, of the coated ceramic is also significantly higher (~10 times) than that of the uncoated ceramic. Figure 5D compares the failure strain and specific energy absorption between the coated and uncoated ceramics, indicating the superior mechanical performance of the coated ceramic to the uncoated counterpart. The above simulation results qualitatively agree well with the experimental results shown in fig. S4.

Figure 5E presents the snapshots of interfacial interaction between the epoxy coating and the ceramic under the uniaxial compression.

There exist large amounts of hydrogen bonds between the ceramic and epoxy coating (as shown in the circular insets in Fig. 5E), which are formed between -NH$_2$ of the epoxy and -OH of the ceramic, as well as -OH of the epoxy and -OH of the ceramic. As a result, the coating of the ceramic with a flexible epoxy via a high-temperature dipping process followed by UV curing leads to a conformal and void-free interface between the epoxy and the ceramic, as also evident in our simulation (Fig. 5E). That is, the surface defects on the ceramic are effectively reduced, if not fully eliminated. For example, the blue rectangles and squares in Fig. 5E highlight the evolution of the interfacial interaction during the compression process, during which the epoxy coating fills in the surface defects in the ceramic and thus effectively reduces stress concentration. The strength of a brittle material (e.g., ceramic) is strongly tied to the size and number of defects (both surface and inner) in the material. Therefore, the strength of the coated ceramic increases significantly. The flexible epoxy polymer has a much larger deformability than the brittle ceramic. When the uncoated ceramic is under large compression, the fracture initiates from surface or internal defects and propagates catastrophically, leading to the brittle fracture of the ceramic. Conversely, when the coated ceramic is under large compression, the fracture initiates from internal defects and propagates to the surface of the ceramic, which could be effectively arrested by the flexible epoxy polymer (Fig. 5E). More fracture initiation and propagation in the ceramic eventually cause the fracture of the epoxy polymer, which leads to a significantly higher failure strain and thus a significantly higher energy absorption.
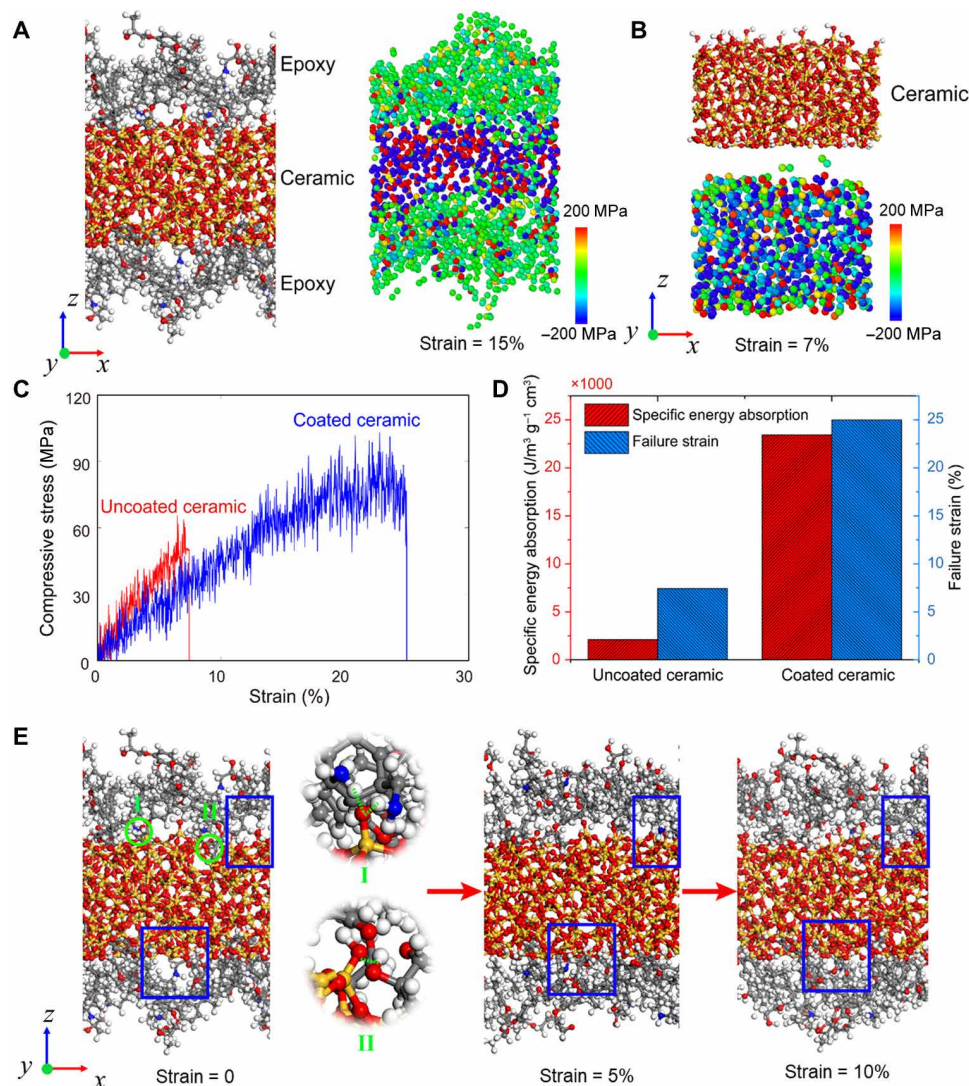
Fig. 5. The simulation models of epoxy-coated and uncoated ceramic and the comparison of their mechanical performance under uniaxial compression. (**A**) Atomic structure and stress distribution of epoxy-coated ceramic under uniaxial compression in the *x* direction. (**B**) Atomic structure and stress distribution of uncoated ceramic under uniaxial compression in the *x* direction. (**C**) Stress-strain curve of coated and uncoated ceramic. (**D**) Specific energy absorption and failure strain of uncoated and coated ceramic. (**E**) Snapshots of epoxy-coated ceramic under uniaxial compression. The circular insets in the second panel show the two types of hydrogen bonds formed between the epoxy and the ceramic (zoom-in view of the green circled regions in the first panel). The upper inset shows the hydrogen bond between -NH$_2$ and -OH, while the lower one shows the hydrogen bond between -OH and -OH. The blue rectangles and squares highlight the evolution of the interfacial interaction during the compressing process, during which the epoxy coating fills in the surface defects of the ceramic and thus effectively reduces stress concentration.

DISCUSSION

In summary, we have printed the architected complex ceramic structure via SLA 3D printing, coated it with a thin polymer coating (~70 to 100 μm), and characterized its mechanical properties. The uniaxial compression test shows multifold improvement in strength and toughness of the coated ceramic geometry as compared to uncoated ceramic one. By in situ micro-CT imaging, we have demonstrated that the polymer micro-coating plays a crucial role in avoiding crack interconnection and propagation. Also, FEM analysis shows the strain accommodation and crack trapping due to the polymer coating. While the effect of micro-coating in crack initiation is not substantial, it considerably delays the damage propagation and catastrophic failure of the ceramic structures. While the effect of the polymer coating is shown to be independent of the structure of the underlying ceramic, the efficacy of the method is more pronounced in architected porous structures compared with their solid dense counterparts in terms of toughness due to their higher surface area. We envisage that our simple approach of externalizing soft phases unlike natural ceramic composite could be extended to many structural applications, where simultaneous optimization of weight and mechanical performance of the ceramic is required.

MATERIALS AND METHODS
Fabrication of ceramic schwarzites

The 3D model of schwarzites structures was generated using Solid-Works, and the printing process was carried out on a Formlabs SLA

printer (Form 2, USA) with a 405-nm laser source. All samples were printed in 1.5 cm^3 with a resolution of 25 μm × 25 μm × 50 μm in the *x*, *y*, and *z* direction, respectively, and each layer was exposed to 44 s of UV light.

The silica-filled (~70% SiO$_2$) preceramic resin (Formlabs Ceramic Resin 1 L, USA) was used to print samples. Details of the resin have been provided in the Supplementary Materials (fig. S10). After printing, all samples were separated from the substrate, subsequently washed in isopropyl alcohol (IPA) for 5 min to remove excess resin from the built part, and then air-dried. Next, according to the post-processing protocol from the supplier, the printed ceramic samples were fired in an actively ventilated furnace with a specific temperature ramp for 28 hours to burn out the binding polymers (debinding process) and sinter the ceramic particle (sintering process) followed by air-cooling to room temperature to achieve the fully ceramic structures. Details regarding the firing process are provided in the Supplementary Materials (fig. S1 and table S1). Note that the structures shrank by around 15% in the *xy* axis and by 29% in the *z* axis during firing. Because of the lower concentration of the ceramic between layers, the structures had higher shrinkage along the printed *z* axis than the *xy* axis.

The printed ceramic samples were then dip-coated with UV-curable flexible epoxy (UV Cure 60-7156, EPOXIES, USA) for a conformal thin coating onto the surface. To confirm the uniform and void-free coating, the dipping method was used in an oven for about 10 min with a temperature of 80°C. Last, all samples were placed under UV light to cure the epoxy for 3 hours.

Scanning electron microscopy

Morphology and fracture surfaces were observed using a field-emission scanning electron microscope (FEI Quanta 400) with a 20-kV accelerating voltage. The surfaces were coated with a thin layer of gold to prevent charging.

Quasi-static mechanical test

Uniaxial compression test was carried out on coated and uncoated ceramic structures at room temperature using a universal testing machine (Instron ElectroPuls E3000, USA) according to ASTM C1424. The crosshead speed was 1.0 mm/min. Load-deflection data for each sample were collected. Note that for the architected ceramic structures, the specimen had a dimension of 1 cm × 1 cm × 1 cm and the area for measuring the stress is determined considering the relative density of the structures (*38*). For solid cylindrical samples, the length-to-diameter ratio was 1.5 to prevent buckling. The specific energy absorption was calculated on the basis of the area under the curve of force-displacement divided by the density of the samples. A minimum of five specimens from each category was tested to ensure the consistency of the data.

Micro-CT imaging

The samples were scanned using a Bruker Skyscan 2211 nano-CT cone-beam scanner (Skyscan, Bruker, Belgium) with x-ray source settings of 65-kV source voltage, 600-μA source current, and 120-ms exposure time. Each sample was measured in microfocus mode using a 3-megapixel active-pixel complementary metal-oxide semiconductor flat panel x-ray detector at a 15-μm voxel resolution. A total of 1042 x-ray projections were collected through a 180° rotation of the sample with a 0.2° angular step size in around 30 min. The acquired images were reconstructed by volumetric NRecon Reconstruction

Software (Skyscan, Bruker, Belgium), which uses a modified Feldkamp algorithm (*39*). During reconstruction, typically occurring artifacts, such as ring artifacts and beam-hardening artifacts, were corrected. The different datasets were reoriented and registered with each other by DataViewer 2D/3D Micro-CT Slice Visualization software (Skyscan, Bruker, Belgium), and the 3D models of the samples were created using CTVox 3D Micro-CT Volume Rendering software (Skyscan, Bruker, Belgium). In situ compression tests were carried out in an MTS2 material testing stage (Skyscan, Bruker, Belgium), which can apply a maximum of 440-N force and is able to measure displacement with a ±0.01-mm accuracy. The samples were measured at five different loads (ranging from 0 to 440 N) to investigate the load-bearing properties and the crack propagation in the different samples.

Finite element method

A 3D faceted model of printed ceramic schwarzite was converted to a solid body using SpaceClaim. To study the effect of coating on damage propagation, we use concrete damaged plasticity model available in the commercial finite element software package ABAQUS/Standard. This model, which was first introduced by Lubliner and coworkers (*40*), has been used to study concrete structures (*41, 42*), but it is also suitable to analyze quasi-brittle materials, including ceramics (*43*). This model considers both tensile and compressive cracking and allows separate tensile and compressive behaviors. Damage is characterized by a scalar degradation variable $d = (1 - d_t)(1 - d_c)$, where d_t and d_c are compressive and tensile degradation variables and are functions of plastic strains. As the material degrades, the elastic modulus of the material decreases. Therefore, the damaged elasticity equations are expressed as

$$\sigma_{ij} = (1 - d)\, C_{ijkl}(\varepsilon_{ij} - \varepsilon_{ij}^p)$$

Two stress invariants are used in flow potential and yield function in this model. A non-associated flow rule is used where the plastic potential function is the Drucker-Prager hyperbolic function. Dilation angle and flow potential eccentricity are two input parameters of the plastic potential function. We assume the values of 31° and 0.1 for dilation angle and flow potential eccentricity, respectively. The yield function used in this model was first introduced by Lubliner *et al.* (*40*) and then modified by Lee and Fenves (*44*). The shape factor and ratio of biaxial to uniaxial compressive strengths are two input parameters that describe yield function, and we set values of 0.66 and 1.16 to them, respectively. It should be mentioned that no qualitative change will be observed in the results presented upon change of input parameters of the model, although results may vary quantitively. We also need to specify values of compressive and tensile degradation damage variables and compressive and tensile yield stresses in terms of inelastic strain. The reader is referred to Abaqus user's manual (*43*) for more information on the model and definitions of inelastic strain. We assume similar behavior in compression and tension and set values listed in tables S4 and S5 for the yield and degradation behavior of the material, where $\overline{\sigma}_y = \frac{\sigma_y}{\sigma_{0y}}$, σ_y is yield stress and $\sigma_{0y} = 90$ MPa. These values have been chosen such that a brittle failure of the ceramic without coating can be observed in about 2% total strain, where total strain is defined as the total change in the height of unit cell divided by its initial length.

Atomistic simulation method

The full atomistic simulation using ReaxFF potential (*45*) implemented in the Large-Scale Atomic/Molecular Massively Parallel Simulator (LAMMPS) (*46*) simulation package is performed to determine the atomic interaction between epoxy and ceramic. The atomic unit structure of diglycidyl ether of bisphenol A (DGEBA) and isophorone diamines (IPD) is obtained by geometry optimization, as shown in figs. S8 and S9 (*47–49*). We then define the reaction groups as R1 and R2 in fig. S8 (A and B). The random crosslink ratio of DGEBA and IPD is set as 10:5 in the box with the size of 28.51 Å × 28.51 Å × 7.687 Å (fig. S8C) to fit the size of amorphous silica (28.51 Å × 28.51 Å × 17.81 Å). The ceramic in the modeling is composed of amorphous silica (SiO_2). The periodic boundary is applied in the x, y, and z directions. Then, we cut the surface of epoxy and coat it on the surfaces of the ceramic, as shown in Fig. 1A. A Nose-Hoover thermostat is used to maintain the NPT ensembles at 300 K in the process of relaxation for 25 ps, which is large enough to relax the coated and uncoated ceramic to the stable state. The densities of the resulting epoxy and ceramic in our simulation are 1.131 g/cm^3 and 1.977 g/cm^3, respectively, which fit well with our experimental data of flexible epoxy (1.1 g/cm^3) and 3D-printed sintered ceramic (1.9 g/cm^3). The timestep is set as 0.5 fs, and the periodical boundary conditions are applied in both x and y directions. Nonperiodic boundary is applied in the z direction, so the surface of the epoxy is free. All the calculations are relaxed using the conjugate gradient algorithm to minimize the total energy of the system until the total atomic forces are converged to less than 10^{-9} eV/Å. In the compressing process, the loading is applied in the x direction, and the NVT ensembles at 300 K are maintained until the structure is broken. The per-atom stress is obtained by averaging the atomic stress in every 500 steps.

SUPPLEMENTARY MATERIALS

Supplementary material for this article is available at http://advances.sciencemag.org/cgi/content/full/7/28/eabc5028/DC1

REFERENCES AND NOTES

1. F. Greco, L. Leonetti, A. Pranno, S. Rudykh, Mechanical behavior of bioinspired nacre-like composites: A hybrid multiscale modeling approach. *Compos. Struct.* **233**, 111625 (2020).
2. F. Song, A. K. Soh, Y. L. Bai, Structural and mechanical properties of the organic matrix layers of nacre. *Biomaterials* **24**, 3623–3631 (2003).
3. J. Gim, N. Schnitzer, L. M. Otter, Y. Cui, S. Motreuil, F. Marin, S. E. Wolf, D. E. Jacob, A. Misra, R. Hovden, Nanoscale deformation mechanics reveal resilience in nacre of *Pinna nobilis* shell. *Nat. Commun.* **10**, 4822 (2019).
4. K. J. Koester, J. W. Ager, R. O. Ritchie, The true toughness of human cortical bone measured with realistically short cracks. *Nat. Mater.* **7**, 672–677 (2008).
5. H. D. Espinosa, J. E. Rim, F. Barthelat, M. J. Buehler, Merger of structure and material in nacre and bone—Perspectives on de novo biomimetic materials. *Prog. Mater. Sci.* **54**, 1059–1100 (2009).
6. R. Wang, H. S. Gupta, Deformation and fracture mechanisms of bone and nacre. *Annu. Rev. Mater. Res.* **41**, 41–73 (2011).
7. P. Fratzl, Biomimetic materials research: What can we really learn from nature's structural materials? *J. R. Soc. Interface* **4**, 637–642 (2007).
8. U. G. K. Wegst, H. Bai, E. Saiz, A. P. Tomsia, R. O. Ritchie, Bioinspired structural materials. *Nat. Mater.* **14**, 23–36 (2015).
9. F. Barthelat, Z. Yin, M. J. Buehler, Structure and mechanics of interfaces in biological materials. *Nat. Rev. Mater.* **1**, 16007 (2016).
10. J. Bauer, S. Hengsbach, I. Tesari, R. Schwaiger, O. Kraft, High-strength cellular ceramic composites with 3D microarchitecture. *Proc. Natl. Acad. Sci. U.S.A.* **111**, 2453–2458 (2014).
11. D. Jang, L. R. Meza, F. Greer, J. R. Greer, Fabrication and deformation of three-dimensional hollow ceramic nanostructures. *Nat. Mater.* **12**, 893–898 (2013).
12. L. M. Rueschhoff, L. A. Baldwin, R. Wheeler, M. J. Dalton, H. Koerner, J. D. Berrigan, N. M. Bedford, S. Seifert, M. K. Cinibulk, M. B. Dickerson, Fabricating ceramic nanostructures with ductile-like compression behavior via rapid self-assembly of block copolymer and preceramic polymer blends. *ACS Appl. Nano Mater.* **2**, 250–257 (2019).
13. T. A. Schaedler, A. J. Jacobsen, A. Torrents, A. E. Sorensen, J. Lian, J. R. Greer, L. Valdevit, W. B. Carter, Ultralight metallic microlattices. *Science* **334**, 962–965 (2011).
14. L. R. Meza, A. J. Zelhofer, N. Clarke, A. J. Mateos, D. M. Kochmann, J. R. Greer, Resilient 3D hierarchical architected metamaterials. *Proc. Natl. Acad. Sci. U.S.A.* **112**, 11502–11507 (2015).
15. L. R. Meza, J. R. Greer, Mechanical characterization of hollow ceramic nanolattices. *J. Mater. Sci.* **49**, 2496–2508 (2014).
16. J. H. Lee, L. Wang, M. C. Boyce, E. L. Thomas, Periodic bicontinuous composites for high specific energy absorption. *Nano Lett.* **12**, 4392–4396 (2012).
17. R. C. Pullar, R. M. Novais, Ecoceramics. *Mater. Today* **20**, 45–46 (2017).
18. P. Calvert, Biomimetic ceramics and composites. *MRS Bull.* **17**, 37–40 (1992).
19. B. Chen, X. Peng, J. G. Wang, X. Wu, Laminated microstructure of Bivalva shell and research of biomimetic ceramic/polymer composite. *Ceram. Int.* **30**, 2011–2014 (2004).
20. H. Sieber, Biomimetic synthesis of ceramics and ceramic composites. *Mater. Sci. Eng. A* **412**, 43–47 (2005).
21. F. Bouville, E. Maire, S. Meille, B. van de Moortèle, A. J. Stevenson, S. Deville, Strong, tough, and stiff bioinspired ceramics from brittle constituents. *Nat. Mater.* **13**, 508–514 (2014).
22. A. Maguire, N. Pottackal, M. A. S. R. Saadi, M. M. Rahman, P. M. Ajayan, Additive manufacturing of polymer-based structures by extrusion technologies. *Oxf. Open Mater. Sci.* **1**, itaa004 (2021).
23. E. Zanchetta, M. Cattaldo, G. Franchin, M. Schwentenwein, J. Homa, G. Brusatin, P. Colombo, Stereolithography of SiOC ceramic microcomponents. *Adv. Mater.* **28**, 370–376 (2016).
24. J. Schmidt, A. A. Altun, M. Schwentenwein, P. Colombo, Complex mullite structures fabricated via digital light processing of a preceramic polysiloxane with active alumina fillers. *J. Eur. Ceram. Soc.* **39**, 1336–1343 (2019).
25. P. Jana, O. Santoliquido, A. Ortona, P. Colombo, G. D. Sorarù, Polymer-derived SiCN cellular structures from replica of 3D-printed lattices. *J. Am. Ceram. Soc.* **101**, 2732–2738 (2018).
26. J. Schmidt, P. Colombo, Digital light processing of ceramic components from polysiloxanes. *J. Eur. Ceram. Soc.* **38**, 57–66 (2018).
27. M. Martín, X. Centelles, A. Solé, C. Barreneche, A. I. Fernández, L. F. Cabeza, Polymeric interlayer materials for laminated glass: A review. *Constr. Build. Mater.* **230**, 116897 (2020).
28. W. Gao, R. Wang, S. Chen, M. Zang, An intrinsic cohesive zone approach for impact failure of windshield laminated glass subjected to a pedestrian headform. *Int. J. Impact Eng.* **126**, 147–159 (2019).
29. S. Chen, M. Zang, D. Wang, S. Yoshimura, T. Yamada, Numerical analysis of impact failure of automotive laminated glass: A review. *Compos. Part B Eng.* **122**, 47–60 (2017).
30. J. P. Gong, Y. Katsuyama, T. Kurokawa, Y. Osada, Double-network hydrogels with extremely high mechanical strength. *Adv. Mater.* **15**, 1155–1158 (2003).
31. S. M. Sajadi, P. S. Owuor, S. Schara, C. F. Woellner, V. Rodrigues, R. Vajtai, J. Lou, D. S. Galvão, C. S. Tiwary, P. M. Ajayan, Multiscale geometric design principles applied to 3D-printed schwarzites. *Adv. Mater.* **30**, 1704820 (2018).
32. S. M. Sajadi, C. S. Tiwary, A. H. Rahmati, S. L. Eichmann, C. J. Thaemlitz, D. Salpekar, A. B. Puthirath, P. J. Boul, M. M. Rahman, A. Meiyazhagan, P. M. Ajayan, Deformation resilient cement structures using 3D-printed molds. *iScience* **24**, 102174 (2021).
33. A. R. Studart, Turning brittleness into toughness. *Nat. Mater.* **13**, 433–435 (2014).
34. R. O. Ritchie, The conflicts between strength and toughness. *Nat. Mater.* **10**, 817–822 (2011).
35. C. Zhang, D. A. Mcadams, J. C. Grunlan, Nano-/micromanufacturing of bioinspired materials: A review of methods to mimic natural structures. *Adv. Mater.* **28**, 6292–6321 (2016).
36. A. Dutta, S. A. Tekalur, Crack tortuousity in the nacreous layer—Topological dependence and biomimetic design guideline. *Int. J. Solids Struct.* **51**, 325–335 (2014).
37. W. J. Clegg, K. Kendall, N. M. Alford, T. W. Button, J. D. Birchall, A simple way to make tough ceramics. *Nature* **347**, 455–457 (1990).
38. L. Gibson, M. Ashby, *Cellular Solids: Structure and Properties,* (Cambridge Solid State Science Series, Cambridge University Press, 1997).
39. L. a Feldkamp, L. G. Davis, J. W. Kress, Practical cone-beam algorithm. *J. Opt. Soc. Am. A* **1**, 612–619 (1984).
40. J. Lubliner, J. Oliver, S. Oller, E. Oñate, A plastic-damage model for concrete. *Int. J. Solids Struct.* **25**, 299–326 (1989).
41. B. L. Wahalathantri, D. P. Thambiratnam, T. H. T. Chan, S. Fawzia, A material model for flexural crack simulation in reinforced concrete elements using Abaqus, in *Proceedings of the First International Conference on Engineering, Designing and Developing the Built Environment for Sustainable Wellbeing* (Queensland University of Technology, 2011), pp. 260–264.
42. A. S. Genikomsou, M. A. Polak, Finite element analysis of punching shear of concrete slabs using damaged plasticity model in ABAQUS. *Eng. Struct.* **98**, 38–48 (2015).
43. Simulia, *ABAQUS 6.14 User's Manuals* (Dassault Systèmes Simulia Corp., 2016).

44. J. Lee, G. L. Fenves, Plastic-damage model for cyclic loading of concrete structures. *J. Eng. Mech.* **124**, 892–900 (1998).

45. A. D. Kulkarni, D. G. Truhlar, S. Goverapet Srinivasan, A. C. T. van Duin, P. Norman, T. E. Schwartzentruber, Oxygen interactions with silica surfaces: Coupled cluster and density functional investigation and the development of a new ReaxFF potential. *J. Phys. Chem. C* **117**, 258–269 (2013).

46. S. Plimpton, Fast parallel algorithms for short-range molecular dynamics. *J. Comput. Phys.* **117**, 1–19 (1995).

47. Z. Wang, Q. Lv, S. Chen, C. Li, S. Sun, S. Hu, Effect of interfacial bonding on interphase properties in SiO2/epoxy nanocomposite: A molecular dynamics simulation study. *ACS Appl. Mater. Interfaces* **8**, 7499–7508 (2016).

48. M. Soleymanibrojeni, H. Shi, F. Liu, E.-H. Han, Effects of surface modification of nano-SiO2 imbedded in organic matrix on interfacial accumulation of water molecules: An atomistic simulation study. *Surf. Interfaces* **23**, 100942 (2021).

49. E. Mounif, V. Bellenger, P. Mazabraud, F. Nony, A. Tcharkhtchi, Chemorheological study of DGEBA/IPD system for reactive rotational molding (RRM). *J. Appl. Polym. Sci.* **116**, 969–976 (2010).

50. Formlabs, 3D Printing Materials: Ceramic Resin; https://formlabs.com/materials/ceramics/.

51. Epoxies, UV Curable Epoxies—Illumabond UV Curable Epoxy Systems.

52. P. Menetrey, K. J. Willam, Triaxial failure criterion for concrete and its generalization. *Struct. J.* **92**, 311–318 (1995).

53. K. J. Willam, Constitutive model for the triaxial behaviour of concrete. *Proc. Intl. Assoc. Bridge Structl. Engrs.* **19**, 1–30 (1975).

54. ANSYS theory manual. ANSYS, Inc., Canonsburg, PA, USA, Release 2019R2 (2019).

55. V. Truxova, J. Safka, M. Seidl, I. Kovalenko, L. Volesky, M. Ackermann, Ceramic 3D printing: Comparison of SLA and DLP technologies. *MM Sci. J.* **2020**, 3905–3911 (2020).

56. W. Nawrot, K. Malecha, Additive manufacturing revolution in ceramic microsystems. *Microelectron. Int.* **37**, 79–85 (2020).

57. Z. Chen, Z. Li, J. Li, C. Liu, C. Lao, Y. Fu, C. Liu, Y. Li, P. Wang, Y. He, 3D printing of ceramics: A review. *J. Eur. Ceram. Soc.* **39**, 661–687 (2019).

58. C. Manière, G. Kerbart, C. Harnois, S. Marinel, Modeling sintering anisotropy in ceramic stereolithography of silica. *Acta Mater.* **182**, 163–171 (2020).

Science Advances

Damage-tolerant 3D-printed ceramics via conformal coating

Seyed Mohammad Sajadi, Lívia Vásárhelyi, Reza Mousavi, Amir Hossein Rahmati, Zoltán Kónya, Ákos Kukovecz, Taib Arif, Tobin Filleter, Robert Vajtai, Peter Boul, Zhenqian Pang, Teng Li, Chandra Sekhar Tiwary, Muhammad M. Rahman and Pulickel M. Ajayan

ARTICLE TOOLS	http://advances.sciencemag.org/content/7/28/eabc5028
SUPPLEMENTARY MATERIALS	http://advances.sciencemag.org/content/suppl/2021/07/02/7.28.eabc5028.DC1
REFERENCES	This article cites 52 articles, 3 of which you can access for free http://advances.sciencemag.org/content/7/28/eabc5028#BIBL
PERMISSIONS	http://www.sciencemag.org/help/reprints-and-permissions

Use of this article is subject to the Terms of Service